Two-dimensional tetrahexagonal CX_2 (X = P, As, Sb) semiconductors for photocatalytic water splitting under visible light

Mehmet Emin Kilic [*]

Computational Science Center, Korea Institute of Science and Technology, Seoul 136-791, Republic of Korea

Soheil Ershad Rad and Seymur Jahangirov [†]

UNAM-Institute of Materials Science and Nanotechnology, Bilkent University, Ankara 06800, Turkey

In this paper, we introduce a family of two-dimensional group-V carbides with an ordered sequence of tetragons and hexagons (*th*-CX_2, where X = P, As, and Sb). We demonstrate that *th*-CX_2 monolayers exhibit robust energetic, dynamical, thermal, and mechanical stability. Our calculations show that the intrinsic structural anisotropy of the *th*-CX_2 family induces strongly anisotropic mechanical, electronic, and optical behavior. These monolayers offer ultrahigh ultimate tensile strength, comparable with that of graphene, making them suitable for strain engineering of electronic and optical properties. They are semiconductors in nature, where *th*-CP_2, *th*-CAs_2, and *th*-CSb_2 possess quasidirect, direct, and indirect band gaps, respectively. The band gaps of *th*-CP_2 and *th*-CAs_2 are wide enough to provide the photogenerated energy required for the splitting of water. Besides, the positions of band edges are in alignment with the water oxidation and reduction potentials. For *th*-CSb_2, however, the suitable width of the band gap and the appropriate band edge positions for photocatalytic water splitting are achieved by strain engineering. Both indirect-to-direct and direct-to-indirect band gap transitions can be induced in *th*-CX_2 compounds through strain engineering. The *th*-CX_2 monolayers offer anisotropic high charge carrier mobility, which prolongs the average lifetime of charge carrier drift. They have good optical absorption ($\sim 10^5$ cm^{-1}) in the visible and ultraviolet regions of the light spectrum. GW_0+BSE (Bethe-Salpeter equation) calculations reveal that they exhibit strong excitonic effects where the first bright excitonic binding energy is calculated as 0.27, 0.52, and 0.22 eV for *th*-CP_2, *th*-CAs_2, and *th*-CSb_2, respectively. Having all these features in one package, the *th*-CX_2 monolayers are among the best candidates for high-performance photocatalytic water splitting.

I. INTRODUCTION

Over the past two decades, two-dimensional (2D) materials have been at the center of attention. In this family of materials, the out of plane quantum confinement results in distinct electronic, mechanical, and optical properties, not present in their bulk counterparts [1,2]. Among these unique features, the extremely high surface to volume ratio combined with shorter charge carrier migration distance has made some of the 2D crystals promising for performance enhancement in hydrogen generation from photocatalytic water splitting [3–5]. Several studies have indicated that 2D materials can outperform their bulk parents in photocatalysis. For instance, it was shown that the photocurrent density produced in 2D SnS$_2$ [6] and ZnSe [7] crystals are 70 and 200 times greater than their bulk form, respectively. Similar efficiency enhancements were also observed in 2D WS$_2$ [8] and CdS [9], relative to their bulk forms. Although these results are promising, there is a long road ahead of 2D materials to achieve the desirable photocatalytic efficiency, and superior candidates should be proposed through experimental and theoretical studies.

The advent of graphene [10–13], in 2004, can be considered as the genesis of the era of 2D materials. In graphene, the presence of two inequivalent Dirac cones at the K and K$'$ corners of the Brillouin zone (BZ) induces defectless ballistic charge transport, making graphene more conductive than copper [14,15]. However, the gapless nature of graphene is an obstacle to its functionality in semiconducting and optical absorption applications [16]. Carbon-based 2D compounds, on the other hand, can simultaneously offer outstanding electrical and mechanical properties, inherited from their graphene parent, and an energy band gap in the semiconducting region. Thus, in the quest for superior 2D materials, carbon-based compounds received significant attention. Since carbon offers different hybridization states, including sp, sp^2, and sp^3, not only formation of different carbon allotropes are possible but also this feature can be utilized in the design of new carbon-based compounds with different chemical and physical properties [17]. Penta-graphene (*p*-C) [18] and tetrahex-carbon (*th*-C) [19], are two recently designed carbon allotropes with sp^2-sp^3 orbital hybridization, which exhibit outstanding electronic, mechanical, and optical properties. *p*-C is the counterpart of graphene with pentagons as its building blocks, offering negative Poisson's ratio and ultrahigh tensile strength. Upon the Stone-Wales transformation, *p*-C makes a structural transition into a more energetically favorable *th*-C

035402-1

(a)   *p*-C**X**₂   **(b)**   *th*-C**X**₂
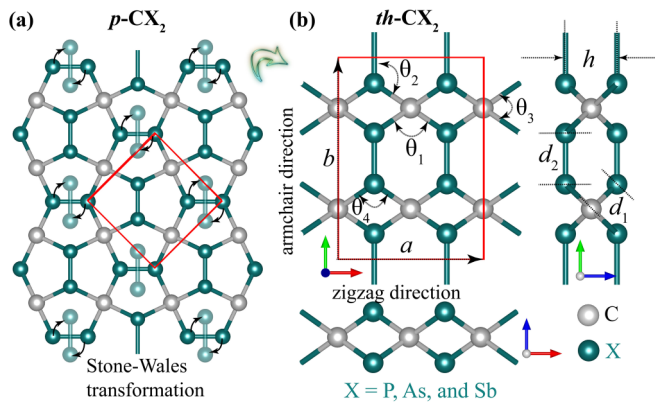

FIG. 1. (a) Ball and stick model of *p*-CX_2 monolayers. Formation of *th*-CX_2 (X = P, As, and Sb) monolayers from *p*-CX_2 through Stone-Wales transformation is illustrated. (b) Top and side views of *th*-CX_2 monolayers. The unit cells of *p*-CX_2 and *th*-CX_2 are shown by red lines. Green and gray balls represent X and C atoms, respectively.

phase [see Fig. 1(a)]. The *th*-C shows a direct band gap, high charge carrier mobility, and anisotropic electronic properties, promising for a nanoelectronic device [20,21]. Although these allotropes of carbon offer some desirable properties in pristine condition, extra functional features can be induced in them through compounding. Very recently, penta-carbides (*p*-XC_2, X = Si, Ge, Sn) have been proposed to be promising candidates for photocatalytic water splitting [22] while their tetrahex counterparts, *th*-XC_2, exhibit narrow direct band gaps with tunable charge carrier mobility, making them suitable for nanolectronic applications [21]. Furthermore, Kilic *et al.* [23] studied the compounds of *th*-C with other group-IV elements, known as *th*-CX (where X = Si, Ge, and alloys). They showed that these compounds are highly stable, satisfying all the requirements needed for synthesis. These compounds offer highly anisotropic mechanical, electronic, and optical properties, and significant potential for photocatalytic water splitting applications. The *p*-CX_2 (where X = P, As, and Sb) family having negative Poisson's ratio, high charge mobility, and strain-tunable properties have also been reported as promising candidates for photocatalytic water splitting [24].

In this paper, using state of the art first-principles methods, we study *th*-CX_2 (where X = P, As, and Sb), a family of 2D materials, that can be formed by the structural transition from *p*-CX_2 compounds [Fig. 1(a) and Fig. S1 of the Supplemental Material [25]]. We first discuss the structural properties of *th*-CX_2 compounds; then we investigate their energetic, vibrational, thermal, and mechanical stability. Later, the most important mechanical properties for strain engineering of these materials are investigated, including Young's modulus, Poisson's ratio, and ultimate tensile strength. Next, electronic band structure and orbital projected density of states are discussed. Finally, we inspect if these materials have the prerequisites for an efficient photocatalytic water splitting. We show that this family satisfies all the essential requirements for this process, including proper band gap width and band alignment with the redox potential of water splitting, prolonged charge carrier lifetime due to anisotropic carrier mobility, and suitable solar light absorption coefficient. Moreover, we demonstrate that via strain engineering other members of this

family can also gain improvement in their photocatalytic water splitting efficiency.

II. METHODS

We performed first principles calculations based on the density functional theory (DFT), using projector-augmented wave potentials [26] and a plane-wave basis set with an energy cutoff of 520 eV. All calculations were performed using the Vienna Ab-initio Simulation Package (VASP) [27,28]. The exchange-correlation potential is approximated by the generalized gradient approximation (GGA) with the Perdew, Burke, and Ernzerhof (PBE) functional [29]. For Brillouin zone integration, a $18 \times 18 \times 1$ Γ-centered k-point grid mesh was used. The equilibrium configuration of atoms and lattice constants were determined by minimizing the total energy of the system using the conjugate gradient method until force components on each atom were decreased below 0.01 eV/Å. To avoid interaction between periodic images in adjacent cells along the z axis, a vacuum spacing of at least 20 Å was inserted, and periodic boundary conditions were applied along the x and y axis. The energy band gap underestimation in the PBE scheme was corrected by the Heyd-Scuseria-Ernzerhof hybrid functional (HSE06), constructed by mixing 25% of nonlocal Fock exchange with 75% of PBE exchange and 100% of PBE correlation energy [30,31]. To examine the dynamical stability of the proposed monolayers, phonon dispersion calculations were performed using the Phonopy package [32]. The lattice dynamics calculations of *th*-CP₂, *th*-CAs₂, and *th*-CSb₂ were carried out with $5 \times 5 \times 1$, $4 \times 4 \times 1$, and $4 \times 4 \times 1$ supercell, respectively, where $2 \times 2 \times 1$ k mesh was adopted to calculate the dynamical matrix, with very high accuracy (the convergence criterion of the total energy was set to 10^{-8} eV). To check the thermal stability of the examined monolayers with a large supercell of $4 \times 3 \times 1$, the *ab initio* molecular dynamics calculations (AIMD) were performed under constant temperature (T) and volume (V), where the temperature was controlled by a Nose thermostat [33]. The total simulation time for the AIMD simulations was taken 14 ps with a time step of 1 fs. For optical response calculations, we employed GW_0 approximation and the Beth-Salpeter equation (BSE) to include electron-hole interactions [34–36], where k-point sampling was limited to $12 \times 12 \times 1$ and the plane-wave cutoff energy was reduced to 480 eV due to the computational limit. However, the total number of bands was increased to 144 since a very large number of empty bands is necessary to converge the quasiparticle energies in the GW_0 approximation.

III. RESULTS AND DISCUSSION

A. Atomic structures

The atomic structure of 2D tetrahexagonal group-V carbides with the formula of *th*-CX_2 (X = P, As, and Sb) is presented in Fig. 1. The monolayers have an orthorhombic unit cell with two unequal lattice constants of a and b, forming a *Cmme* symmetry (space group no. 67). The structures are made of two inequivalent atomic sites, with different coordination numbers, where the fourfold coordinated positions are occupied by carbon atoms and the threefold coordinated

TABLE I. Structural, energetic, and electronic properties of th-CX_2 compounds and their penta counterparts (p-CX_2), where a and b are the lattice parameters, h is the thickness, d_1 is the bond length between fourfold coordinated and threefold coordinated atoms in units of Å, d_2 is the dimer bond length in units of Å, $\theta_{(1-4)}$ are the interbond angles, E_{coh} is the cohesive energy in units of eV/atom, and E_g^{PBE} and E_g^{HSE} are the band gap energies in units of eV obtained from the PBE and HSE06 functional methods, respectively. E_{VBM} and E_{CBM} are the energy levels of the valence band maximum and conduction band minimum with respect to vacuum level in units of eV calculated through the HSE06 method. The vacuum level is set to 0 eV. For the sake of comparison, the corresponding properties of th-XC$_2$ monolayers and their penta counterparts (p-XC$_2$) are also presented where X = Si, Ge, and Sn.

Structure	a	b	h	d_1	d_2	θ_1	θ_2	θ_3	θ_4	E_{coh}	E_g^{PBE}	E_g^{HSE}	E_{VBM}	E_{CBM}	Type
th-CP$_2$	5.31	7.20	2.32	1.88	2.28	139	110	90	90	4.61	1.26	2.12	−6.01	−3.89	Quasidirect
th-CAs$_2$	5.60	8.00	2.52	2.02	2.55	138	111	92	88	4.56	1.52	2.31	−5.82	−3.51	Direct
th-CSb$_2$	6.10	9.10	2.81	2.22	2.96	138	111	93	87	3.76	0.60	1.15	−5.06	−3.91	Indirect
p-CP$_2$[a]	4.09	4.09	1.61	1.88	2.28						1.78	2.64	−6.09	−3.45	Indirect
p-CAs$_2$[a]	4.36	4.09	2.50	2.02	2.65						1.41	2.09	−5.46	−3.37	Indirect
p-CSb$_2$[a]	4.79	4.09	2.81	2.21	2.97						0.80	1.35	−4.70	−3.34	Indirect
th-C[b]	4.53	6.11	1.16	1.339	1.54	112	124	85	95		1.62	2.63	−4.93	−2.30	Direct
th-SiC$_2$[c]	5.52	7.20	1.34	1.352	1.90	108	126	87	93			−0.01	−2.61	−2.62	Direct
th-GeC$_2$[c]	5.93	7.34	1.42	1.339	2.01	109	125	85	95		0.17	0.87	−2.95	−2.08	Direct
th-SnC$_2$[c]	6.59	7.94	1.42	1.331	2.23	107	126	85	95			0.15	−2.17	−2.03	Direct
p-C[d]	3.64	3.64	1.21	1.34	1.55						2.38	3.26	−5.08	−1.83	Indirect
p-SiC$_2$[d]	4.41	4.41	1.33	1.36	1.91						1.49	2.39	−5.84	−3.44	Indirect
p-GeC$_2$[d]	4.60	4.60	1.37	1.34	2.01						1.60	2.23	−5.42	−3.19	Indirect
p-SnC$_2$[d]	5.05	5.05	1.39	1.34	2.22						1.02	1.36	−4.35	−2.99	Indirect

[a]Reference [24].
[b]Reference [17].
[c]Reference [21].
[d]Reference [22].

locations are filled by the group-V elements, denoted by C and X, respectively. Accordingly, the structures are made of three atomic layers, where the layer made of C atoms is sandwiched between two layers of X atoms, and the distance between the top and bottom layers defines the thickness, denoted by h. The bond lengths between C–X and X–X are represented by d_1 and d_2, respectively. The combination of the tetragonal and hexagonal building blocks in the th-CX_2 monolayers results in peculiar mechanical, electronic, and optical properties, which can be exploited in various applications, such as in nanoelectronics, optoelectronics, and especially photocatalytic water splitting.

The structural parameters of th-CX_2 monolayers are summarized in Table I and, for the sake of comparison, properties of p-CX_2 (X = P, As, Sb) [24], th-C [17], th-XC$_2$ (X = Si, Ge, Sn) [21], p-C, and p-XC$_2$ (X = Si, Ge, Sn) [22] are also presented. As the atomic radius of the group-V elements increases, the lattice constants in both directions expand, in a way that the ratio between them remains almost constant. For the same reason, the bond lengths show a similar increasing trend. For th-CP$_2$, the obtained lattice constants are $a = 5.31$ Å, $b = 7.20$ Å, and the layer thickness is found to be $h = 2.32$ Å. The C–P bond length ($d_1 = 1.88$ Å) is exactly the same as its counterpart in p-CP$_2$ (1.88 Å) [24,37]. The calculated P–P bond length of 2.28 Å is almost the same as in black phosphorus (2.25–2.28 Å) [38]. In the case of th-CAs$_2$, the elongation in the structure expands the lattice constants into $a = 5.60$ Å, $b = 8.00$ Å, and $h = 2.52$ Å. Similarly, the bond length of C–As ($d_1 = 2.02$ Å) is precisely equal to its counterpart in p-CAs$_2$ [39]. The same rules apply to th-CSb$_2$ with $a = 6.10$ Å, $b = 9.10$ Å, and $h = 2.81$ Å, where C–Sb bond length ($d_1 = 2.22$ Å) is compatible with C–Sb bond

length ($d_1 = 2.21$ Å) in p-CSb$_2$. These structural properties show that carbon atoms exhibit an sp^3 orbital hybridization and participate in four σ bonds with surrounding X atoms. We further calculated the electron localization function (ELF), providing a good description of electron localization and chemical bonding character in materials. The ELF of th-CX_2 monolayers is presented in Fig. S2 of the Supplemental Material [25]. We observed that the electrons in th-CX_2 are well localized around the X atoms and the C–X and X–X bonds, suggesting strong covalent bonding. Electronegativity difference between carbon and group-V elements also corroborates the covalent nature. The electronegativity of carbon is higher than that of X atom; consequently, the X–X bonds are slightly longer than their average value for a single bond.

B. Energetic stability

We evaluate the thermodynamic stability of th-CX_2 monolayers by calculating the cohesive energies (E_{coh}) and the formation energies (E_f) and comparing them to similar structures that have already been shown to be stable. Here, the E_{coh} and E_f can be extracted from the following expressions;

$$E_{coh} = \frac{n_C E_C + n_X E_X - E_{CX_2}}{n_C + n_X} \qquad (1)$$

and

$$E_f = \frac{E_{CX_2} - n_C E(C) - n_X E(X)}{n_C + n_X}, \qquad (2)$$

where E_{CX_2} is the total energy of one unit cell of th-CX_2 sheet and E_C and E_X are the energies of isolated C and X atoms, respectively; n_C and n_X are the numbers of C and X atoms per
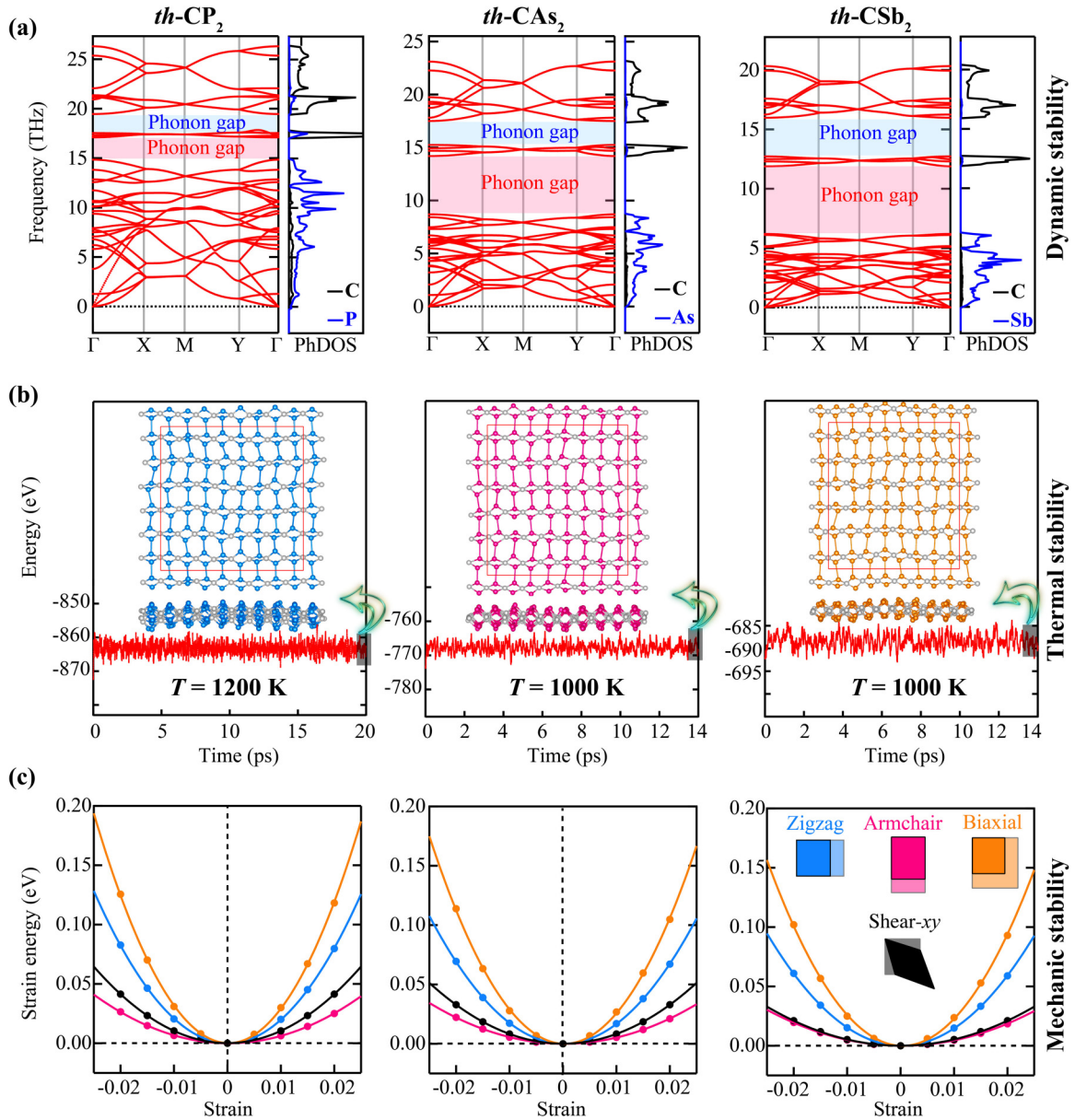
FIG. 2. (a) Phonon spectrum with atom-projected phonon density of states (PhDOS) of the *th*-CX_2 compounds. (b) Variation of the potential energy during the AIMD simulations at 1000 K (1200 K for *th*-CP$_2$) for a period of 14 ps (20 ps for *th*-CP$_2$). The insets are snapshots of the atomic structures at the end of the AIMD simulations. The blue, pink, orange, and gray balls represent P, As, Sb, and C atoms, respectively. (c) Variation of strain energy with respect to zigzag, armchair, equibiaxial, and shear strains. The strain energy of the equilibrium structures is set to 0 eV.

unit cell; the $E(C)$ and $E(X)$ are the total energies per atom for graphene and molecular X_2, respectively. It can be inferred that high enough E_{coh} and low formation energy imply the relative energetic stability of the system. The cohesive energies of *th*-CX_2 monolayers are listed in Table I. By comparing the cohesive energies of *th*-CX_2 monolayers with that of graphene (7.94 eV/atom) [10], *th*-C (7.12 eV/atom) [19], and *p*-C (7.09 eV/atom) [18], we can see that *th*-CX_2 monolayers have less favorable cohesive energies. However, the cohesive energies of *th*-CX_2 surpass that of already synthesized silicene (4.70 eV/atom) [40], germanene (4.15 eV/atom) [41], and phosphorene (3.48 eV/atom) [42]. The *th*-CX_2 cohesive energy values lie in the range of synthesized structures, which is a sign that *th*-CX_2 structures are strongly bonded. Moreover, the

calculated formation energies of *th*-CX_2 monolayers are 100, 140, and 190 meV per atom for $X =$ P, As, and Sb, respectively. These low formation energies for *th*-CX_2 monolayers suggest their thermodynamic stability.

C. Dynamic stability

The dynamic stability of the *th*-CX_2 monolayers were studied based on their phonon dispersions calculated via *abinitio* lattice dynamics. The dispersions of phonon modes with atom-projected density of states (PhDOS) are depicted in Fig. 2(a). The 12 atoms are presented in a unit cell of *th*-CX_2, each having three vibrational degrees of freedom, constituting a total of 36 phonon modes, of which three are

acoustic branches with zero frequency at Γ point. In all 2D monolayers, the transverse acoustic (TA) and longitudinal acoustic (LA) branches exhibit a linear dispersion around the Γ point, while the out-of-plane acoustic (ZA) branch has a quadratic dispersion in the long wavelength limit. Based on the harmonic approximation, imaginary frequencies are the manifestation of a disassembling vibrational mode. Hence the prerequisite of dynamic stability is that all phonon modes must have real (positive) frequencies. We note that, as the lattice dynamics calculations were performed using the supercell approach, we tested the size of supercell for the th-CP$_2$ monolayer, of which phonon dispersion curves for 2×2, 3×3, 4×4, and 5×5 supercells are presented in Fig. S3 of the Supplemental Material [25]. The phonon dispersion curves of th-CP$_2$ with 2×2 and 3×3 supercells have imaginary frequencies, while that with a 4×4 supercell exhibits very small imaginary frequency or seems to be flatness ZA branch near the Γ point. Normally, such imaginary or flatness frequency of ZA branch in the phonon dispersion curves is expected for 2D materials, and disappeared with the increase of the supercell size. As we expect, th-CP$_2$ with the 5×5 supercell is free from imaginary frequencies. We ascertain that 5×5, 4×4, and 4×4 supercells for th-CP$_2$, th-CAs$_2$, and th-CSb$_2$ monolayers, respectively, are large enough to obtain the converged lattice dynamics results (i.e., the interaction between equivalent atoms and the force constants at the supercell boundary are negligible). This analysis heralds the dynamical stability of th-CX_2 structures. PhDOS analysis reveals that high phonon frequencies are mainly contributed by the vibrations of C atoms, while the low phonon frequencies are produced by the vibrations of X atoms, resulting from the large difference in mass between C and X atoms. Moreover, the high phonon frequency of the X atom decreases when moving from P to Sb. As seen in Fig. 2(a), the width of the phononic gap increases with the increase of mass difference between C and X atoms in th-CX_2 monolayers.

D. Thermal stability

To verify the thermal stability of th-CX_2 monolayers, *ab initio* molecular dynamics simulations (AIMD) were performed at high temperature for a duration of 14 ps. To reduce the periodic boundary condition constraints on the structure and provide a suitable condition for any possible reconstruction, a $4 \times 3 \times 1$ supercell was employed. Snapshots of the final atomic configuration of the structures at the end of the AIMD simulation and the diagrams of the potential energy variation vs time are provided in Fig. 2(b). We found that th-CP$_2$ lose their structural integrity at $T = 1400$ K and th-CAs$_2$ and th-CSb$_2$ become fragmented at $T = 1200$ K. Thus, in our simulation, we considered $T = 1200$ K for th-CP$_2$ and $T = 1000$ K for th-CAs$_2$ and th-CSb$_2$. It can be seen that the potential energies only fluctuate during the simulation without any considerable deviation, which implies that no reconstruction takes place. These fluctuations are the result of the thermal oscillations of the atoms around their equilibrium positions. From the snapshots of the ultimate arrangement of the atoms, it can be inferred that none of the bonds are broken at the elevated temperatures and the original skeleton of the structures is preserved. It should be mentioned that

the computational considerations limit the AIMD simulations to a few ps, which is a short interval in real conditions, but it can provide an insight into the system's thermal stability, especially structural response to thermal shock.

E. Mechanical stability

According to the Born-Huang elastic stability criteria [43], the prerequisites of the mechanical stability of the considered systems are $C_{11}C_{22}$-$C_{12}^2 > 0$ and $C_{66} > 0$, where C_{11}, C_{22}, C_{12}, and C_{66} are the elastic stiffness constants. These constants can be calculated by fitting the strain energy (E_s) per unit area into a function of the in-plane strains using the following equation:

$$E_s(\varepsilon) = \tfrac{1}{2}C_{11}\varepsilon_x^2 + \tfrac{1}{2}C_{22}\varepsilon_y^2 + C_{12}\varepsilon_x\varepsilon_y + 2C_{66}\varepsilon_{xy}^2, \quad (3)$$

where ε_x, ε_y, and ε_{xy} are the infinitesimal uniaxial strains along the zigzag (**a**) and armchair (**b**) directions, and shear strain, respectively. To extract the elastic stiffness constants, the corresponding strains were applied in a range of -2% to 2% with an increment of 0.5%. The variation in strain energy vs strain is demonstrated in Fig. 2(c). In case of uniaxial strain along **a** lattice vector (where $\varepsilon_y = \varepsilon_{xy} = 0$),

$$E_s(\varepsilon) = \tfrac{1}{2}C_{11}\varepsilon_x^2, \quad (4)$$

for uniaxial strain along **b** lattice vector (where $\varepsilon_x = \varepsilon_{xy} = 0$),

$$E_s(\varepsilon) = \tfrac{1}{2}C_{22}\varepsilon_y^2, \quad (5)$$

if we apply equibiaxial strain (where $\varepsilon_x = \varepsilon_y$ and $\varepsilon_{xy} = 0$),

$$E_s(\varepsilon) = \left(\tfrac{1}{2}C_{11} + \tfrac{1}{2}C_{22} + C_{12}\right)\varepsilon_x^2, \quad (6)$$

and finally in case of shear strain (where $\varepsilon_x = \varepsilon_y = 0$),

$$E_s(\varepsilon) = 2C_{66}\varepsilon_{xy}^2. \quad (7)$$

Therefore, from Eq. (4), C_{11} can be obtained by applying strain along lattice vector **a** (where $\varepsilon_x = \frac{a-a_0}{a_0}$ and $\varepsilon_y = 0$). Similarly, from Eq. (5), C_{22} can be calculated by applying uniaxial strain along lattice vector **b** (where $\varepsilon_y = \frac{b-b_0}{b_0}$ and $\varepsilon_x = 0$). Having C_{11} and C_{22}, to find C_{12} from Eq. (6) equibiaxial strain can be employed (where $\varepsilon_x = \varepsilon_y$). We note that a_0 (b_0) and a (b) are the equilibrium and strained lattice constants along the zigzag (armchair) direction. Finally, from Eq. (7), C_{66} can be extracted by applying shear strain where the uniaxial strain along **a** and **b** lattice vectors are zero ($\varepsilon_x = \varepsilon_y = 0$) [see the inset of Fig. 2(c)]. We note that, in case of uniaxial strains, a perpendicular stress component will appear in the system due to the Poisson effect. This stress was relieved by structural relaxation along that axis. We also note that $\varepsilon_{xy} = \varepsilon_{yx}$ for the monolayers is confirmed by the variation of strain energy with respect to uniaxial shear strains, namely Shear-x and Shear-y (Fig. S4 of the Supplemental Material [25]). The obtained elastic constants are listed in Table II. The obtained elastic constants meet Born-Huang elastic stability criteria for every member of the th-CX_2 family.

F. Mechanical properties

Having secured that all members of the th-CX_2 family have energetic, dynamical, thermal, and mechanical stability, we investigated the most important strain-dependent mechanical properties of these materials, including in-plane

TABLE II. Mechanical properties of th-CX_2 monolayers and their penta counterparts, where C_{ij} are the elastic stiffness constants in units of N/m, Y_a and Y_b are the Young's moduli along zigzag and armchair directions in units of N/m, ν_a and ν_b are the Poisson's ratios along zigzag and armchair directions, and UTS$_a$, UTS$_b$, and UTS$_{ab}$ are the ultimate tensile strain under zigzag, armchair, and equibiaxial strains in %, respectively. For the sake of the comparison, the corresponding properties of th-XC$_2$ monolayers and their penta counterparts (p-XC$_2$) are also presented where $X =$ Si, Ge, and Sn.

	Mechanical constants (N/m)				Young's modulus (N/m)		Poisson's ratio		Ultimate tensile strain (%)		
	C_{11}	C_{22}	C_{12}	C_{66}	Y_a	Y_b	ν_a	ν_b	UTS$_a$	UTS$_b$	UTS$_{ab}$
th-CP$_2$	170.14	54.00	15.42	21.61	168.75	49.60	0.09	0.28	17	27	18
th-CAs$_2$	121.80	38.70	17.30	14.63	119.34	30.96	0.14	0.45	18	27	17
th-CSb$_2$	86.44	27.49	13.33	7.59	84.38	21.02	0.15	0.48	17	24	16
p-CP$_2$[a]	84.11	84.11	44.72	79.18	60.33	60.33	0.53	0.53	24	24	18
p-CAs$_2$[a]	63.77	63.77	41.07	61.46	37.32	37.32	0.64	0.64	27	27	18
p-CSb$_2$[a]	40.78	40.78	36.20	44.94	8.65	8.65	0.89	0.89	30	30	18
th-C[b]	287.03	280.82	16.21	123.99	286.12	279.88	0.06	0.06	32	31	20
th-SiC$_2$[c]	99.85	104.47	45.03	55.94	79.55	85.06	0.45	0.43	27	26	20
th-GeC$_2$[c]	125.36	112.22	14.17	47.93	123.76	110.43	0.11	0.13	18	18	13
th-SnC$_2$[c]	88.80	68.35	14.51	21.79	86.42	65.27	0.16	0.21	13	19	12
p-C[d]	267.54	267.54	−18.81	150.95	266.22	266.22	−0.070	−0.070	17	17	21
p-SiC$_2$[d]	138.71	138.71	4.82	73.01	138.54	138.54	0.035	0.035	21	21	16
p-GeC$_2$[d]	122.24	122.24	8.48	63.60	121.65	121.65	0.069	0.069	16	16	12
p-SnC$_2$[d]	83.83	83.83	14.76	44.49	81.23	81.23	0.176	0.176	9	9	7

[a]Reference [24].
[b]Reference [17].
[c]Reference [21].
[d]Reference [22].

Young's modulus (Y_{2D}), Poisson's ratio (ν), and ultimate tensile strength. As it is shown in the following sections, the intrinsic anisotropy in the geometric structure of th-CX_2 gives rise to direction-dependent mechanical properties.

1. Young's modulus

Young's modulus is the slope of the stress-strain curve in the elastic region which defines the stiffness of the material. A material with high stiffness deforms slightly under stress. Since structural deformation can dramatically change the electronic and optical properties, stiffness is of great importance in the study of 2D materials. The intrinsic anisotropy in the geometric structure of th-CX_2 gives rise to the direction-dependent Young's modulus. Here, through the following expression, we represent the angle-dependent Young's modulus of th-CX_2 compounds,

$$Y_{2D}(\theta) = \frac{C_{11}C_{22} - C_{12}^2}{C_{11}A^4 + \left(\frac{C_{11}C_{22}-C_{12}^2}{C_{66}} - 2C_{12}\right)A^2B^2}, \quad (8)$$

where A and B stand for $\sin(\theta)$ and $\cos(\theta)$, respectively. In Fig. 3(a), Y_{2D} of th-CX_2 compounds vs in-plane angle (θ) is presented. Other than the intrinsic asymmetry of the structure, the unequal strength of the dominant bonds in the armchair and zigzag directions directly affects the stiffness anisotropy. This difference stems from the variation in bond length and hybridization of states. In the th-CX_2 structures, along the

zigzag direction ($\theta = 0°$ and due to reflection symmetry $\theta = 180°$), where C–X bonds are dominant, materials exhibit superior stiffness compared to the armchair direction ($\theta = 90°$ and due to reflection symmetry $\theta = 270°$), where X–X bonds are dominant. The numerical value of Y_{2D} of th-CX_2 along $\theta = 0°$ (denoted as Y_a) and $\theta = 90°$ (denoted as Y_b) directions are listed in Table II. For the sake of comparison, Young's moduli of similar structures are summarized in Table II. It can be seen that the maximum Y_{2D} of th-CP$_2$ (169 N/m), th-CAs$_2$ (119 N/m), and th-CSb$_2$ (84 N/m) are almost 3, 3, and 10 times that of their penta counterparts (60, 37, and 9 N/m [24], respectively).

2. Poisson's ratio

When materials are stretched in one direction they usually get thinner in the perpendicular direction. Poisson's ratio (PR) is found by dividing the amount of this thinning to the stretching. Generally, materials possess positive PR, getting thinner upon tensile and thicker under compressive stresses. Although rare, there are some materials with negative PR (known as auxetic) which can offer exotic mechanical properties [44,45]. Similar to other mechanical properties of the th-CX_2 compounds, Poisson's ratio also exhibits a direction-dependent behavior due to the intrinsic anisotropy of the structure. Here, the angle-dependent PR of th-CX_2 compounds was investigated through the following equation:

$$\nu(\theta) = \frac{C_{12}(A^4 + B^4) - \left(C_{11} + C_{22} - \frac{(C_{11}C_{22}-C_{12}^2)}{C_{66}} - 2C_{12}\right)A^2B^2}{C_{11}A^4 + C_{22}B^4 + \left(\frac{(C_{11}C_{22}-C_{12}^2)}{C_{66}} - 2C_{12}\right)A^2B^2}, \quad (9)$$
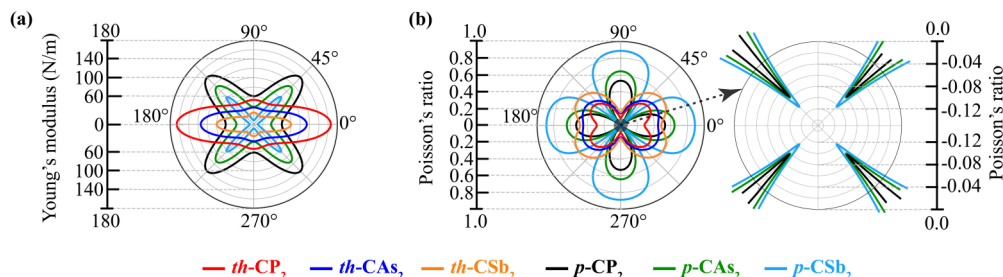
FIG. 3. Orientation-dependent variation of (a) Young's modulus and (b) Poisson's ratio in th-CX_2 monolayers and their penta counterparts (p-CX_2), where $X =$ P, As, Sb.

where A and B stand for $\sin(\theta)$ and $\cos(\theta)$, respectively. The resulted graph of ν vs θ is presented in Fig. 3(b), and the numerical value of PR along $\theta = 0°$ (denoted as ν_a) and $\theta = 90°$ (denoted as ν_b) directions are listed in Table II. It can be seen that th-CX_2 compounds have positive PR, whereas their penta counterparts (p-CX_2) exhibit auxetic behavior with negative PR [see Fig. 3(b), left panel]. We found that the minimum value of ν takes place along the armchair direction ($\theta = 90°$), while the maximum value of ν locates in the range of $0° < \theta \leqslant 45°$. The PR variation of the system is also dependent on the atomic species. As the atomic number increases, the average value of PR shows an increasing trend, which is also the case for the penta counterparts.

3. Ultimate tensile strength

Another mechanical feature of a 2D material, which is of great importance, is ultimate tensile strength. During the strain engineering of a 2D material, extreme strains can be imposed into the system. If the material lacks the proper strength, its structural integrity can be damaged, and the desired performance cannot be achieved. To investigate the ultimate tensile strength of th-CX_2, we employed a $2 \times 2 \times 1$ supercell

and measured the stress imposed into the system upon various axial tensile strains (zigzag, armchair, and equibiaxial). The stress-strain curve for th-CX_2 compounds is depicted in Figs. 4(a)–4(c), where the ultimate tensile strength is the maximum strength that the system tolerates right before the failure. The percentage of strain at the maximum stress known as ultimate tensile strain (UTS) is indicated by the vertical dashed line and, for the sake of comparison, the obtained UTS values of other tetrahex and their penta counterparts for zigzag, armchair, and equibiaxial strains (denoted by UTS$_a$, UTS$_b$, and UTS$_{ab}$, respectively) are summarized in Table II.

From the stress-strain curves, it can be noted that th-CP_2, th-CAs_2, and th-CSb_2 compounds undergo plastic deformation upon tensile strain along the armchair direction before reaching the ultimate tensile strength point. We further probed the atomic origin of this plastic behavior. By comparing the bond lengths in the elastic and plastic regions of the curves (see Fig. S5 of the Supplemental Material [25]), we found that the main reason behind the plastic behavior of the th-CX_2 compounds under armchair strain is the capability of X–X bonds, oriented along the armchair direction, to tolerate significant elongations without detaching. In the case of strain along the zigzag direction, C–X bonds elongation mainly
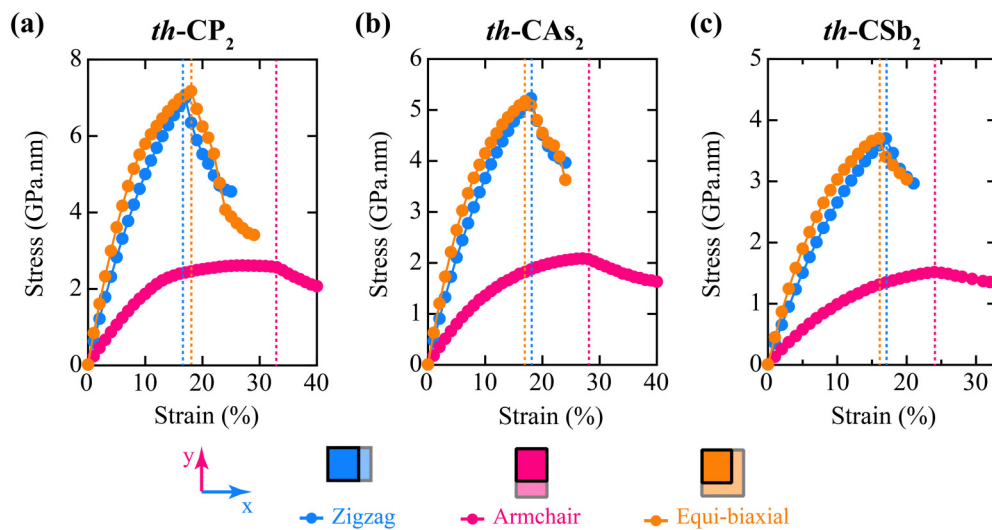

FIG. 4. Calculated stress-strain curves for th-CX_2 compounds subjected to zigzag, armchair, and equibiaxial tensile strains. The percentage of strain at the maximum stress point known as ultimate tensile strain (UTS) is indicated by the vertical dashed line. UTS$_a$, UTS$_b$, and UTS$_{ab}$ refer to the UTS for zigzag, armchair, and equibiaxial tensile strains, respectively.
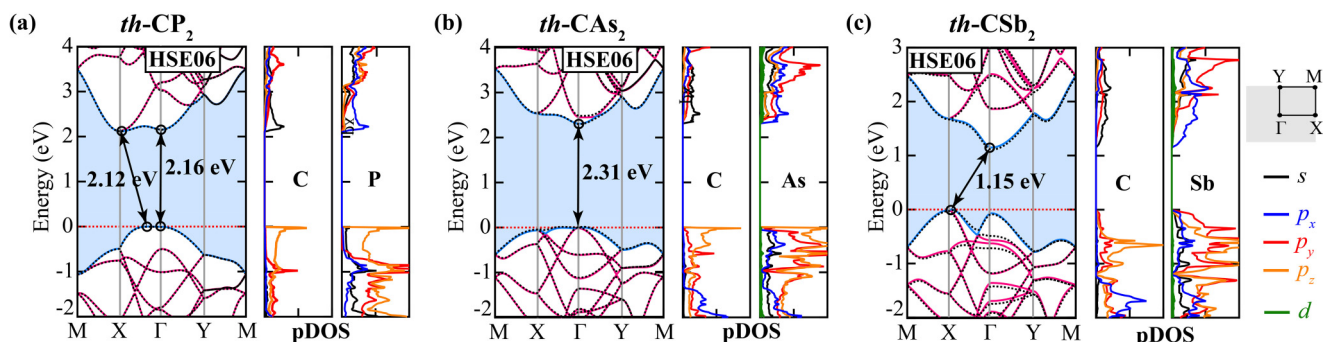
FIG. 5. Electronic band structures obtained from the HSE06 functional for (a) *th*-CP$_2$, (b) *th*-CAs$_2$, and (c) *th*-CSb$_2$ monolayers. The band gap energies between valence band maximum (VBM) and conduction band minimum (CBM) are shown with the black arrows. The fundamental bands gap between VBM and CBM are shaded in blue. The Fermi level (demonstrated by the dashed red line) is set to 0 eV. Bands calculated including and excluding SOC are shown by dashed and solid lines, respectively. The orbital decomposed projected density of states (pDOS) plots are depicted next to their corresponding band structure.

compensate the strain applied to the structure. These bonds elongate linearly up to the ultimate tensile strength point and, after this point, the slope of the curve decreases, showing the bond-breaking mechanism at the maximum stress point. In the case of armchair strain, the *X*–*X* bonds' elongation is not linear up to the UTS point and, between yield strength point and UTS, their expansion accelerates, indicating a plastic behavior. Finally, after the UTS point, the rate of elongation changes which shows their detachment. In the case of equibiaxial strain, we have a combination of the previous mechanisms, where the change in the ratio of bond elongation clearly specifies the maximum stress point. The UTS$_{ab}$ of graphene, *p*-C, *th*-C, and *th*-BN was reported to be 27% [46], 21% [18,22], 20% [23], and 27% [47], respectively. It can be seen that *th*-C*X*$_2$ compounds exhibit ultrahigh ultimate strain, comparable with that of graphene, and outweighing that of PG, satisfying the prerequisite for strain engineering of electronic and optical properties, which will be discussed in the following sections.

G. Electronic structures

Since the PBE approach underestimates the band gap energies, the electronic band structures of the *th*-C*X*$_2$ compounds were calculated using the HSE06 functional and the results are presented in Fig. 5. The band gap energies for both PBE and HSE06 methods are listed in Table I for comparison. It can be seen that all the band gaps lie within the semiconducting range, promising potential for applications in solar cell and photocatalysis. Although the band gap of *th*-CP$_2$ is indirect the energy difference between direct and indirect gaps are so narrow (0.04 eV) that its band gap nature can be considered as quasidirect. The band gap of *th*-CP$_2$ (2.12 eV) is 0.52 eV lower than its penta counterparts (*p*-CP$_2$). For *th*-CAs$_2$, it shows a direct band gap of 2.31 eV where the valence band maximum (VBM) and the conduction band minimum (CBM) are located at Γ, while its penta counterpart has an indirect band gap of 2.09 eV. We note that the quasidirect band gap of 2.12 eV and direct band gap of 2.31 eV for *th*-CP$_2$ and *th*-CAs$_2$, respectively, are comparable with the direct band gap of *th*-C (2.63 eV) [23], making them a competitive alternative of the *th*-C, as one of the best options for nano- and optoelectronic applications. *th*-CSb$_2$ is found to be an indirect

band gap semiconductor with the band gap of 1.15 eV. The band gap energy of *th*-CSb$_2$ is 0.2 eV lower than its penta counterpart (*p*-CSb$_2$). Although SOC lifts the degeneracy, the band gap width and band edge alignments change only marginally (in the order of meV). Based on the pDOS results, it can be inferred that the orbital contributions to valence and conduction bands in *th*-CP$_2$ and *th*-CAs$_2$ show similarities, where the valence band is mostly made of both C and *X* atom p_z states, and the conduction band is a combination of *s* orbital of C and p_x of *X*. In the case of *th*-CSb$_2$, the valence band is mostly made of p_y orbital states of Sb and the conduction band mainly consists of *s* orbital of C and p_x orbital of Sb.

H. Photocatalytic properties for water splitting

To have an efficient photocatalyst for water splitting, a semiconductor needs to satisfy several prerequisites simultaneously [48]. First, the band gap energy should be less than 3 eV to have the optimum solar light absorption. Secondly, to be able to provide enough energy to break covalent bonds of water, the band gap energy must exceed 1.23 eV (the free energy of water splitting) (see Fig. 6). The third crucial
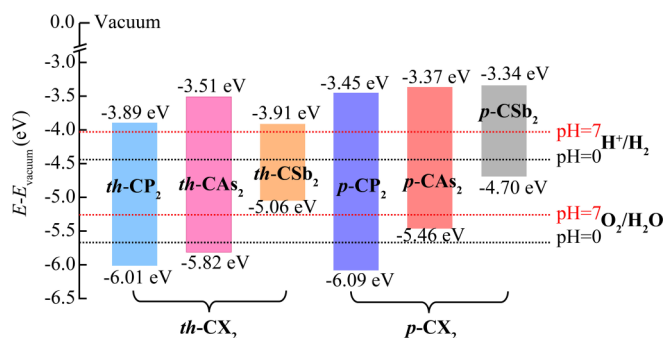

FIG. 6. Location of the band edges in *th*-C*X*$_2$ and their penta counterparts (*p*-C*X*$_2$) with respect to the vacuum level obtained from HSE06 functional. The vacuum level is set to 0 eV. The dashed lines are aligned to the oxidation/reduction potentials of water splitting, where black and red dashed lines denote pH = 0 and pH = 7, respectively.

requirement is the suitable location of band edges with respect to the oxidation/reduction potential of water splitting. In other words, the valence band edge location in the energy spectrum needs to be lower than the oxidation potential of O_2/H_2O (-5.67 eV $+$ pH $\times$ 0.059 eV), and the conduction band edge position must exceed the reduction potential of H^+/H_2 (-4.44 eV $+$ pH $\times$ 0.059 eV) [49]. Photoinduced electron/hole pair will drift for an average lifetime of τ before being annihilated by an exciton pair. To secure an efficient photocatalysis process, the fourth essential feature is a prolonged average lifetime of the charge carriers. To achieve this last requirement, the photogenerated electron/hole pairs should get separated to prevent quick recombination of them, and it is the difference in the relative drift velocities (υ_d) of electron and hole that induces this separation. Mobility, which itself is a function of effective mass, has a direct relation with drift velocity ($\upsilon_d = \mu E$, where E is the electric field). Accordingly, semiconductors that have in-equivalent electron and hole mobility offer a longer charge carrier lifetime. Moreover, a system with direction-dependent mobility can also further facilitate charge carrier separation.

Our first principles calculations reveal that th-CP$_2$ and th-CAs$_2$ monolayers are two suitable candidates that ideally satisfy all of the above mentioned requirements. In this respect, the energy band gap of 2.12/2.16 eV (indirect/direct) and 2.31 eV (direct) for th-CP$_2$ and th-CAs$_2$, respectively, sits ideally within the $1.23 < E_{\text{gap}} < 3.00$ eV range, fulfilling the energy demand for splitting water molecules and offering the optimum solar light absorption simultaneously. As it is summarized in Table I and demonstrated in Fig. 6, the energy level of VBM for th-CP$_2$ and th-CAs$_2$ is calculated as -6.01 eV and -5.82 eV, respectively, which are below the oxidation potential of water (for a whole range of pH $= 0$ to pH $= 7$). Also, the CBM of both candidates are well above the reduction potential (for a whole range of pH $= 0$ to pH $= 7$). Hence th-CP$_2$ and th-CAs$_2$ monolayers present suitable band edges and offer adequate driving force for water splitting. According to the band gap energy and band edge positions, we can firmly claim that th-CP$_2$ and th-CAs$_2$ are excellent candidates for photocatalytic water splitting applications. In the case of th-CSb$_2$, the energy level of CBM (-3.91 eV) is much more positive than the reduction potential of water at pH $= 0$ and pH $= 7$ by 0.53 eV and 0.12 eV, respectively. Unfortunately, the energy level of VBM (-5.06 eV) exceeds the oxidation potential of water splitting at pH $= 0$ and pH $= 7$ by 0.61 eV and 0.20 eV, respectively. In other words, although the CBM of th-CSb$_2$ has the necessary driving force for the reduction reaction, the VBM cannot satisfy the oxidation potential of O_2/H_2O in the range from pH $= 0$ to pH $= 10$. Nevertheless, there is an opportunity to tune the band edge positions of th-CSb$_2$ by controlling the pH to match the redox potential of water. At a basic condition (pH > 10), th-CSb$_2$ has the minimum required driving force for the water-splitting oxidation process. Another effective way to tune the band edge alignment and the band gap energy for th-CSb$_2$ is strain engineering. We discuss the variation of band edges with respect to strain in the following subsection, but, in short, we achieve a larger direct band gap than the minimum energy required for the water splitting reaction and an acceptable band edge alignment for water splitting under 4% biaxial strain. As a consequence, not only th-CP$_2$ and th-CAs$_2$, but also th-CSb$_2$ can be considered potential candidates for water splitting.

I. Strain engineering of the band gap and band edge positions of th-CX_2 compounds

Numerous studies showed that the intrinsic properties of 2D materials can be remarkably improved by structure tailoring. Recently, it was shown that the electronic properties of tetrahexagonal monolayers are sensitive to chemical functionalization, alloying, and mechanical strain [17,47,50,51]. Here, we investigate the effect of strain on the th-CX_2 compounds. Our results obtained using the HSE06 functional are presented in Fig. 7 for zigzag, armchair, and equibiaxial strains within the -4% and 10% range with increments of 2%. A structural relaxation was performed at each step of straining and the electronic properties were calculated for the relaxed structure. It can be seen that, within this strain range, although band gap energies vary significantly, the semiconducting nature of the compounds is preserved and no gap closure is observed. Previously, we demonstrated that th-CP$_2$ and th-CAs$_2$ both offer suitable features for photocatalytic water splitting in pristine condition. These promising features of th-CP$_2$ only miss one property to become ideal, which is the lack of a direct band gap. In pristine condition, the band gap of th-CP$_2$ can be considered to be quasidirect; however, a quasidirect to direct transition can be induced through strain engineering to further boost its photocatalytic efficiency. This transition occurs upon 2% zigzag and biaxial tensile strain. According to Fig. 7(a), under intense biaxial tensile strain, the CBM alignment of th-CP$_2$ with reduction potential of water deteriorates. A similar trend can also be observed in the CBM alignment of th-CAs$_2$, if the armchair tensile strain exceeds 6% [see Fig. 7(b)]. On the other hand, tensile strain along the zigzag direction does not break the alignment of band edges with water decomposition potentials in both of these compounds. Therefore, alongside th-CAs$_2$ in pristine condition, we can consider the strain-engineered versions of th-CP$_2$ as the optimum candidates for photocatalytic water splitting. Finally, in th-CSb$_2$, where an efficient band alignment is not achievable in pristine condition, small tensile strains can enhance the position of the band edges with respect to redox potentials of water, and increase the band gap energy to a near 1.23 eV threshold to provide enough energy for water decomposition. Besides, under tensile strains, an indirect to direct band gap transition can also be induced. Thus a significant improvement can be achieved in photocatalytic efficiency of th-CSb$_2$ for water splitting purposes.

J. Effective mass and carrier mobility

To achieve a better insight into the charge carrier migration properties, the effective mass (m^*) and carrier mobility (μ) of the th-CX_2 compounds are investigated. The effective mass of charge carriers was obtained through fitting a parabolic function into the electronic band structure via the following equation:

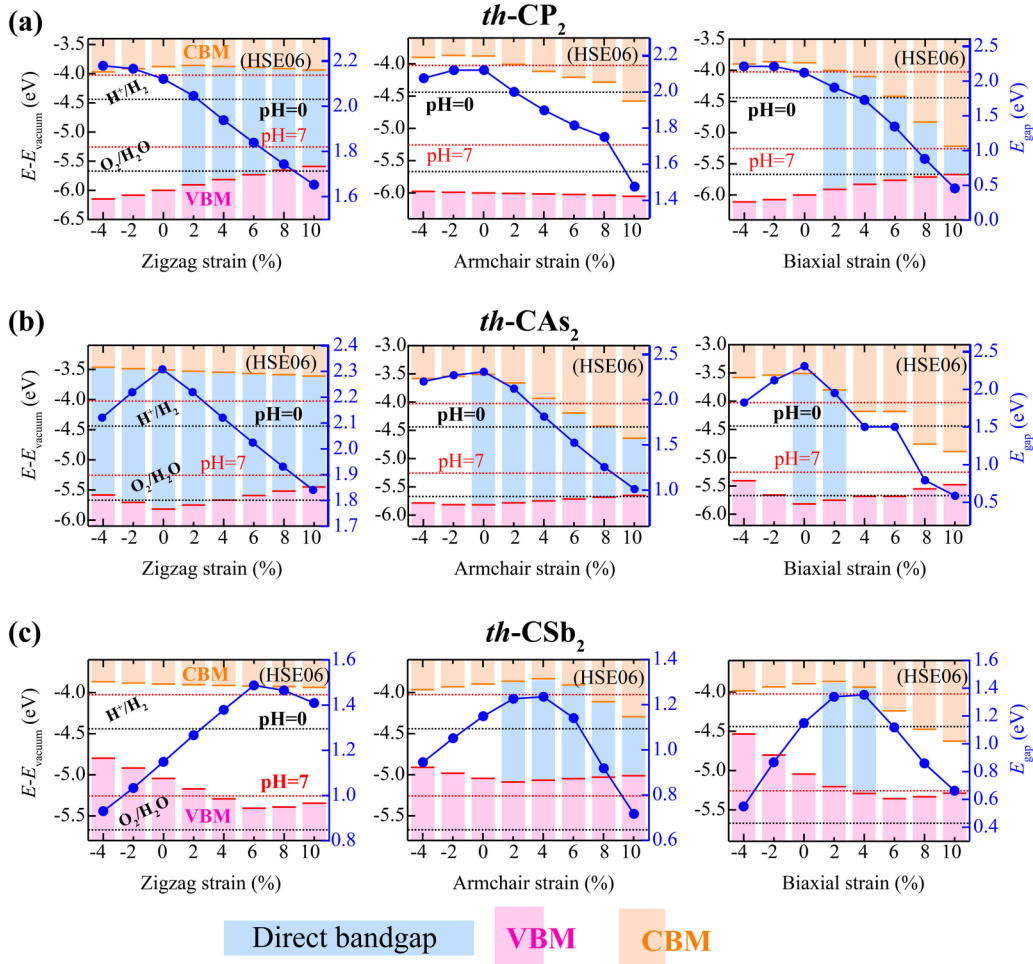$$m^* = \hbar^2 \left(\frac{d^2 E(k)}{dk^2} \right)^{-1}, \qquad (10)$$

FIG. 7. Strain engineering of the band gap and the band edge alignments (with respect to the redox potential of water splitting) of *th*-CX_2 compounds, calculated via HSE06 functional, for zigzag, armchair, and equiiaxial strains in the range of −4% to 10% (negative/positive numbers refer to the compressive/tensile strain), with increments of 2%. The dark blue markers correspond to the band gap values. The valence band maximum (VBM) and conduction band minimum (CBM) positions with respect to the redox potential of water splitting are accentuated with pink and orange tints, respectively. The bright blue shadows indicate the presence of a direct band gap.

where $\hbar$ is the reduced Planck constant, k is the wave vector, and $\frac{d^2E(k)}{dk^2}$ is the second derivative of the energy with respect to the wave vector at the minimum of the conduction band for electrons or the maximum of the valence band for holes. The electron and hole effective masses with respect to

free-electron mass (m_0) along the Γ-X (denoted by m_x^*) and Γ-Y (denoted by m_y^*) are listed in Table III. Moreover, we calculated the direction dependent effective mass of holes and electrons from Γ to an arbitrary direction A. In Fig. 8, it can be seen that the effective masses of electrons and holes are

TABLE III. Charge carrier properties, where m_i^*/m_0 is the carrier effective masses with respect to a static electron mass (m_0) along the i transport direction. C_i is the elastic constant in units of N/m, $E_{d,i}$ is the deformation potential constant in units of eV, and μ_i^{2D} is the carrier mobility in units of cm^{2}V^{-1}s^{-1} at $T = 300$ K.

| Structure	Carrier type	Effective masses		Elastic constants		DP constants		Mob. $\times 10^3$ [Eq. (11)]		Mob. $\times 10^3$ [Eq. (13)]	
		m_x^*/m_0	m_y^*/m_0	C_{2D}^x	C_{2D}^y	$E_{d,x}$	$E_{d,y}$	μ_x^{2D}	μ_y^{2D}	μ_x^{2D}	μ_y^{2D}
th-CP$_2$	Hole	9.22	1.37	170.15	54.00	4.64	0.46	0.01	1.13	0.01	0.08
	Electron	0.89	0.69	170.15	54.00	1.32	6.41	3.02	0.05	0.33	0.18
th-CAs$_2$	Hole	0.54	4.08	121.80	38.70	3.25	1.54	0.31	0.06	0.35	0.05
	Electron	0.58	0.88	121.80	38.70	0.97	1.98	6.79	0.33	2.51	0.91
th-CSb$_2$	Hole	0.19	0.71	86.44	27.49	6.60	2.81	0.59	0.28	0.69	0.21
	Electron	0.25	1.12	86.44	27.49	0.45	1.64	68.12	0.37	11.59	1.18
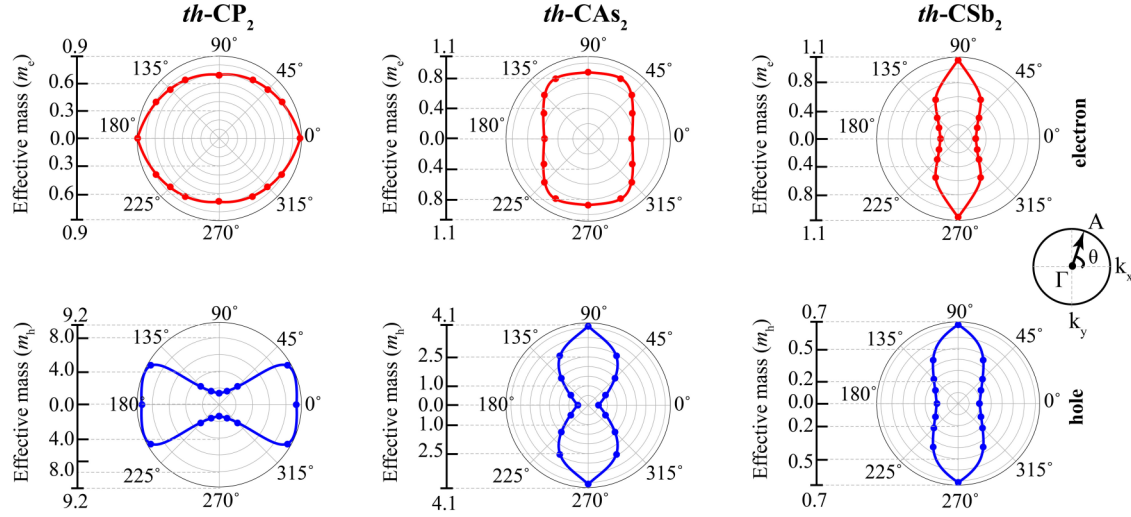
FIG. 8. Direction dependent effective masses in the unit of free electron mass for electrons (upper panel) and holes (lower panel) calculated using energy dispersion from Γ to a nearby point A.

inequivalent and direction dependent in all th-CX_2 compounds. This anisotropy is also manifested in the unequal curvature of band dispersion around the Γ point of the highest valence band and lowest conduction band. We further investigated the charge carrier mobility along the Γ-X (symbolized by μ_x^{2D}) and Γ-Y (symbolized by μ_y^{2D}) directions using the modified Bardeen-Shockley's formula for anisotropic 2D semiconductors [52],

$$\mu_i^{2D} = \frac{e\hbar^3 C_i}{k_B T m_i^* m_d E_{d,i}^2},\qquad(11)$$

where i determines the transport direction (x and y stand for zigzag and armchair, respectively), m_i^* is the effective mass along i direction, and m_d is the geometric mean of effective masses along x and y direction ($\sqrt{m_x^* m_y^*}$). Temperature (T) is considered to be 300 K. $E_{d,i}$ is the deformation potential constant of the carrier, obtainable from the following equation:

$$E_{d,i} = \frac{\Delta E}{\left(\frac{\Delta l}{l_0}\right)},\qquad(12)$$

where ΔE is the variation in the energy of the CBM and VBM bands under small strains (0.5% in our calculations) (see Fig. S(6-9) of the Supplemental Material [25]). The calculated values for $E_{d,i}$ are summarized in Table III. The C_i in Eq. (11) is the in-plane stiffness constant listed in Table III. In Eq. (11), it was assumed that mobility is only dependent on the deformation potential constants, effective masses, and in-plane stiffness constants along the migration direction. In real 2D anisotropic materials, however, mobility is under the influence of scattering events from all directions. This oversimplification can lead to an overestimation of the anisotropic behavior of 2D materials. An improved version of the mobility formula was proposed by Lang $et\ al.$ [53] as follows:

$$\mu_i = \frac{e\hbar^3\left(\frac{5C_i + 3C_j}{8}\right)}{k_B T (m_i^*)^{3/2}(m_j^*)^{1/2}\left(\frac{9E_{d,i}^2 + 7E_{d,i}E_{d,j} + 4E_{d,j}^2}{20}\right)}.\qquad(13)$$

For the sake of comparison, the results obtained from Eq. (13) are also presented in Table III. Results obtained using Eq. (13) have two main differences compared to the corresponding values found from Eq. (11). First, the mobility values resulting from Eq. (13) are relatively lower than the ones obtained from Eq. (11). Secondly, the anisotropy of the mobility obtained from Eq. (13) are lower than their counterparts calculated based on Eq. (11). These deviations stem from the consideration of the effect of electron-phonon scattering events in transpose direction, perpendicular to that of mobility measurement, implemented in Lang $et\ al.$'s formula [Eq. (13)]. Previous studies have shown that Eq. (11) overestimates both the carrier mobility and anisotropic ratio. Equation (13), however, underestimates the carrier mobility while the anisotropy ratios obtained from this formula are in good agreement with experimental results [52]. Thus we estimate that the experimental carrier mobilities of the th-CX_2 compounds settle between the two reported values and the anisotropy is close to the values obtained by Lang $et\ al.$'s method.

K. Optical properties

Optical absorption is another factor that plays a crucial role in the photocatalytic capacity of a material. From an energetic point of view, ultraviolet light can facilitate photocatalytic activities better than visible light, since its high photonic energy is enough to overcome large energy barriers in a catalysis process. On the other hand, the ultraviolet part of the solar spectrum is only limited to 4%. Thus a good photocatalyst also needs to be able to absorb a significant fraction of the visible light (which covers around 43% of the solar radiation, reaching the earth's surface). The light-harvesting performances of th-CX_2 compounds were evaluated by the optical absorption coefficient derived from the dielectric functions [54]:

$$\alpha(\omega) = \sqrt{2}\omega\left\{\sqrt{\varepsilon_1^2(\omega) + \varepsilon_2^2(\omega)} - \varepsilon_1(\omega)\right\}^{1/2},\qquad(14)$$

where $\varepsilon_1(\omega)$ and $\varepsilon_2(\omega)$ are the real and imaginary parts of the dielectric functions, respectively. By employing GW_0+RPA
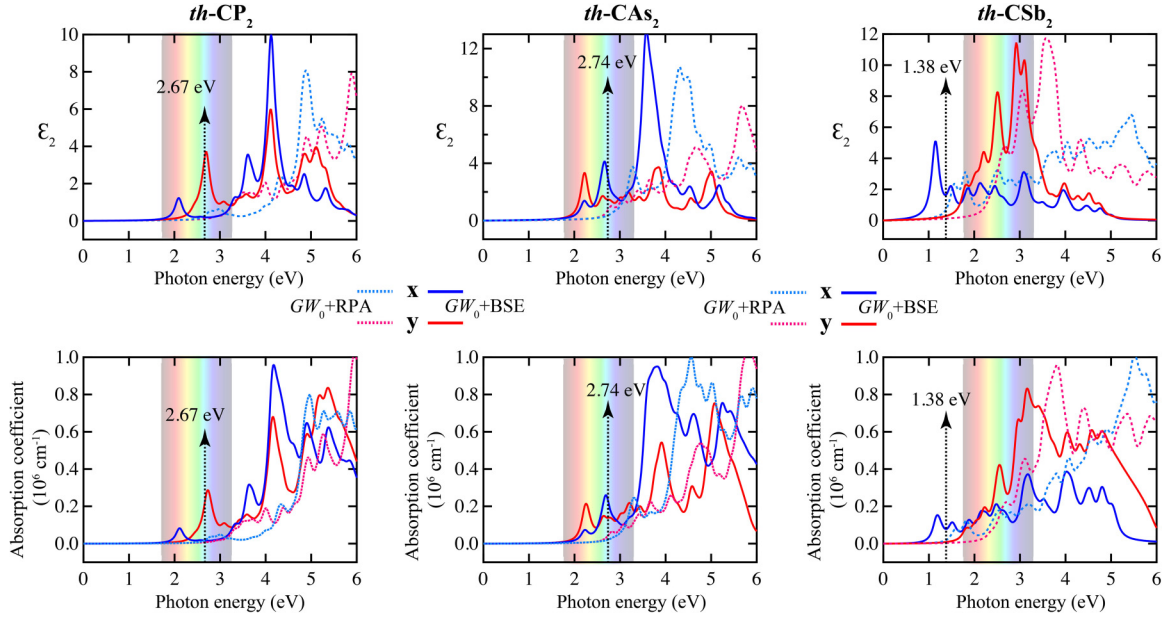
FIG. 9. Optical absorption coefficient of th-CX_2 compounds along zigzag (x) and armchair (y) directions, as a function of photon energy. GW_0+RPA calculation results are depicted by dashed sky blue and pink colors, while GW_0+BSE calculation results are shown by blue and red line colors. The quasiparticle (QP) band gaps, calculated from GW_0 without e-h interactions, are illustrated by black dashed arrows.

and GW_0+BSE approximations, we calculated the dielectric functions and extracted the optical absorption coefficients. Figure 9 shows the imaginary parts of the dielectric functions and optical absorption spectra of th-CX_2 compounds where the polarization vectors are considered parallel to the layer plane (x is along the zigzag edge and y is along the armchair edge). In all of the 2D th-CX_2 compounds the absorption peaks spread all over the visible and ultraviolet spectrum where the optical absorption coefficient can reach 10^{-6} cm^{-1}, which is comparable to that of perovskite solar cells [55]. Anisotropic optical response is clearly seen as a manifestation of the intrinsic anisotropy in the atomic structure. This can be exploited in optoelectronic devices to manipulate the polarization of the incident light. The anisotropic and high optical absorption capacity, combined with the proper band gap and band alignment of th-CX_2 monolayers, make them promising candidates as photocatalysts in the water-splitting process.

The difference between GW_0+RPA and GW_0+BSE optical absorption spectrum is the evidence of the quantum confinement effect in the 2D th-CX_2 compounds. GW_0+RPA method includes electron-electron (e-e) interactions and neglects electron-hole (e-h) interactions, while GW_0+BSE goes beyond RPA by including e-e and e-h interactions. We observed that the e-h interactions dominate the optical absorption spectrum in th-CX_2 monolayers, resulting in the redshift of the spectra with respect to those calculated without e-h interactions. More importantly, the prominent absorption peaks below the quasiparticle (QP) band gap (presented in Fig. 9) determine the main optical features and are only detected with the inclusion of e-h interactions via the GW_0+BSE approximation. The first optical absorption peak occurs at 2.40 eV, 2.22 eV, and 1.16 eV along the zigzag direction for th-CP$_2$, th-CAs$_2$, and th-CSb$_2$, respectively. These peaks are smaller than the fundamental QP band gap obtained from GW_0 calculation

neglecting e-h interactions and hence are interpreted as the first bright exciton peaks.

We extract the excitonic binding energy (E_b) of the first bright exciton using the following equation:

$$E_b = E_g(\text{QP}) - E_{\text{exciton}}, \qquad (15)$$

where $E_g(\text{QP})$ is the GW_0 QP band gap energy and E_{exciton} is the exciton energy obtained from the GW_0+BSE spectrum. The calculated E_b is 0.27, 0.52, and 0.22 eV for th-CP$_2$, th-CAs$_2$, and th-CSb$_2$, respectively. Interestingly, th-CX_2 compounds have large excitonic binding energies, comparable to those of monolayer WS$_2$ (0.32 eV) [56] and many MXenes [57].

IV. CONCLUSION

Using first-principles calculations, we investigated a family of 2D carbides, compounded with group-V dimers. Based on their cohesive energy, phonon spectrum, AIMD simulations, and elastic stability criteria, we revealed that th-CX_2 monolayers are energetically, dynamically, thermally, and mechanically stable. The intrinsic structural anisotropy of these monolayers creates unique direction-dependent mechanical, electronic, and optical properties contrary to their penta counterparts (p-CX_2). th-XC$_2$ monolayers show anisotropic Young's modulus and Poisson's ratio, and ultrahigh ultimate tensile strength, making them suitable for strain engineering. These monolayers are natural semiconductors with desirable band gaps for nanoelectronics and optoelectronics. th-CP$_2$, th-CAs$_2$, and th-CSb$_2$ show quasidirect, direct, and indirect band gap natures, respectively. They have a band gap that lies in the suitable region of the solar spectrum for optimum light absorption, which is simultaneously wide enough to provide sufficient photogenerated energy to overcome the potential barrier of water splitting. They show tunable direct band gaps

and indirect-to-direct (or direct-to-indirect) band gap transitions via strain engineering. Their high anisotropic charge carrier mobility provides the ability for exciton separation and prolongs the average lifetime of electron-hole pairs. Among these 2D carbides, in pristine condition, *th*-CP$_2$ and *th*-CAs$_2$ have the proper band alignment with the oxidation/reduction potential of water splitting. Moreover, this alignment can be improved in *th*-CSb$_2$ through strain manipulation of the electronic properties. The calculated optical band gap is 2.40, 2.22, and 1.16 eV, and the binding energy of the first bright exciton is 0.27, 0.52, and 0.22 eV for *th*-CP$_2$, *th*-CAs$_2$, and *th*-CSb$_2$, respectively. Thus *th*-CX_2 monolayers exhibit strong excitonic effects. Accordingly, we claim that 2D *th*-CX_2 compounds are among the best candidates for high-performance photoinduced catalysis of the water-splitting process.

[1] S. Das, J. A. Robinson, M. Dubey, H. Terrones, and M. Terrones, Annu. Rev. Mater. Res. **45**, 1 (2015).

[2] S. Cahangirov, H. Sahin, G. Le Lay, and A. Rubio, *Introduction to the Physics of Silicene and other 2D Materials* (Springer, New York, 2016), Vol. 930.

[3] Z. Guo, J. Zhou, L. Zhu, and Z. Sun, J. Mater. Chem. A **4**, 11446 (2016).

[4] A. K. Singh, K. Mathew, H. L. Zhuang, and R. G. Hennig, J. Phys. Chem. Lett. **6**, 1087 (2015).

[5] B. Luo, G. Liu, and L. Wang, Nanoscale **8**, 6904 (2016).

[6] Y. Sun, H. Cheng, S. Gao, Z. Sun, Q. Liu, Q. Liu, F. Lei, T. Yao, J. He, and S. Wei, Angew. Chem. Int. Ed. **51**, 8727 (2012).

[7] Y. Sun, Z. Sun, S. Gao, H. Cheng, Q. Liu, J. Piao, T. Yao, C. Wu, S. Hu, and S. Wei, Nat. Commun. **3**, 1 (2012).

[8] D. Voiry, H. Yamaguchi, J. Li, R. Silva, D. C. Alves, T. Fujita, M. Chen, T. Asefa, V. B. Shenoy, and G. Eda, Nat. Mater. **12**, 850 (2013).

[9] Y. Xu, W. Zhao, R. Xu, Y. Shi, and B. Zhang, Chem. Commun. **49**, 9803 (2013).

[10] K. S. Novoselov, A. K. Geim, S. V. Morozov, D. Jiang, Y. Zhang, S. V. Dubonos, I. V. Grigorieva, and A. A. Firsov, Science **306**, 666 (2004).

[11] K. S. Novoselov, A. K. Geim, S. V. Morozov, D. Jiang, M. I. Katsnelson, I. Grigorieva, S. Dubonos, and A. A. Firsov, Nature (London) **438**, 197 (2005).

[12] Y. Zhang, Y.-W. Tan, H. L. Stormer, and P. Kim, Nature (London) **438**, 201 (2005).

[13] A. K. Geim and K. S. Novoselov, Nature Materials **6**, 183 (2007).

[14] P. R. Wallace, Phys. Rev. **71**, 622 (1947).

[15] F. Schwierz, Nat. Nanotechnol. **5**, 487 (2010).

[16] X. Li, J. Yu, S. Wageh, A. A. Al-Ghamdi, and J. Xie, Small **12**, 6640 (2016).

[17] M. E. Kilic and K.-R. Lee, Carbon **161**, 71 (2020).

[18] S. Zhang, J. Zhou, Q. Wang, X. Chen, Y. Kawazoe, and P. Jena, Proc. Natl. Acad. Sci. U.S.A. **112**, 2372 (2015).

[19] B. Ram and H. Mizuseki, Carbon **137**, 266 (2018).

[20] F. M. de Vasconcelos, A. G. Souza Filho, V. Meunier, and E. C. Girão, Carbon **167**, 403 (2020).

[21] M. E. Kilic and K.-R. Lee, Carbon **181**, 421 (2021).

[22] M. E. Kilic and K.-R. Lee, Phys. Rev. Materials **5**, 065404 (2021).

[23] M. E. Kilic and K.-R. Lee, Carbon **174**, 368 (2021).

[24] S. Sun, F. Meng, Y. Xu, J. He, Y. Ni, and H. Wang, J. Mater. Chem. A **7**, 7791 (2019).

[25] See Supplemental Material at http://link.aps.org/supplemental/10.1103/PhysRevMaterials.6.035402. Stone Wales transformation; electron localization functions; phonon dispersion curves; strain energy vs strain; variation of bond lengths with respect to strain; deformation potential constants.

[26] P. E. Blöchl, Phys. Rev. B **50**, 17953 (1994).

[27] G. Kresse and D. Joubert, Phys. Rev. B **59**, 1758 (1999).

[28] G. Kresse and J. Hafner, J. Phys.: Condens. Matter **6**, 8245 (1994).

[29] J. P. Perdew, K. Burke, and M. Ernzerhof, Phys. Rev. Lett. **77**, 3865 (1996).

[30] J. Heyd, G. E. Scuseria, and M. Ernzerhof, J. Chem. Phys. **118**, 8207 (2003).

[31] J. Paier, M. Marsman, K. Hummer, G. Kresse, I. C. Gerber, and J. G. Ángyán, J. Chem. Phys. **124**, 154709 (2006).

[32] L. Chaput, A. Togo, I. Tanaka, and G. Hug, Phys. Rev. B **84**, 094302 (2011).

[33] S. Nosé, J. Chem. Phys. **81**, 511 (1984).

[34] G. Onida, L. Reining, and A. Rubio, Rev. Mod. Phys. **74**, 601 (2002).

[35] S. Albrecht, L. Reining, R. Del Sole, and G. Onida, Phys. Rev. Lett. **80**, 4510 (1998).

[36] M. Rohlfing and S. G. Louie, Phys. Rev. Lett. **81**, 2312 (1998).

[37] M. Naseri, S. Lin, J. Jalilian, J. Gu, and Z. Chen, Front. Phys. **13**, 138102 (2018).

[38] V. Eswaraiah, Q. Zeng, Y. Long, and Z. Liu, Small **12**, 3480 (2016).

[39] M. Naseri, Appl. Surf. Sci. **423**, 566 (2017).

[40] N. D. Drummond, V. Zólyomi, and V. I. Fal'ko, Phys. Rev. B **85**, 075423 (2012).

[41] S. Cahangirov, M. Topsakal, E. Aktürk, H. Şahin, and S. Ciraci, Phys. Rev. Lett. **102**, 236804 (2009).

[42] V. Vierimaa, A. V. Krasheninnikov, and H.-P. Komsa, Nanoscale **8**, 7949 (2016).

[43] M. Born and K. Huang, *Dynamical Theory of Crystal Lattices* (Clarendon Press, Oxford, 1954).

[44] R. Lakes, Science **238**, 551 (1987).

[45] G. N. Greaves, A. Greer, R. S. Lakes, and T. Rouxel, Nat. Mater. **10**, 823 (2011).

[46] F. Liu, P. Ming, and J. Li, Phys. Rev. B **76**, 064120 (2007).

[47] M. E. Kilic and K.-R. Lee, Nanoscale **13**, 9303 (2021).

[48] T. Takata, J. Jiang, Y. Sakata, M. Nakabayashi, N. Shibata, V. Nandal, K. Seki, T. Hisatomi, and K. Domen, Nature (London) **581**, 411 (2020).

[49] V. Chakrapani, J. C. Angus, A. B. Anderson, S. D. Wolter, B. R. Stoner, and G. U. Sumanasekera, Science **318**, 1424 (2007).

[50] M. E. Kilic and K.-R. Lee, J. Phys. Chem. C **124**, 8225 (2020).

[51] M. E. Kilic and K.-R. Lee, J. Mater. Chem. C **9**, 4971 (2021).

[52] A. Rawat, N. Jena, and A. De Sarkar, J. Mater. Chem. A **6**, 8693 (2018).

[53] H. Lang, S. Zhang, and Z. Liu, Phys. Rev. B **94**, 235306 (2016).

[54] S. Saha, T. P. Sinha, and A. Mookerjee, Phys. Rev. B **62**, 8828 (2000).

[55] M. Shirayama, H. Kadowaki, T. Miyadera, T. Sugita, M. Tamakoshi, M. Kato, T. Fujiseki, D. Murata, S. Hara, T. N. Murakami *et al.*, Phys. Rev. Appl. **5**, 014012 (2016).

[56] A. Chernikov, T. C. Berkelbach, H. M. Hill, A. Rigosi, Y. Li, O. B. Aslan, D. R. Reichman, M. S. Hybertsen, and T. F. Heinz, Phys. Rev. Lett. **113**, 076802 (2014).

[57] Z. Jiang, Z. Liu, Y. Li, and W. Duan, Phys. Rev. Lett. **118**, 266401 (2017).